Elastic scattering of ^{58}Ni+^{27}Al at near-barrier energies

M. E. Brandan, J. R. Alfaro, and A. Menchaca-Rocha
Instituto de Física, Universidad Nacional Autónoma de México, A.P.20-364, México 01000 D.F., Mexico

J. Gómez del Campo, G. R. Satchler, P. H. Stelson,* H. J. Kim, and D. Shapira
Physics Division, Oak Ridge National Laboratory, Oak Ridge, Tennessee 37831-6373
(Received 22 February 1993)

The elastic angular distributions for ^{58}Ni+^{27}Al have been measured at five energies from $E_{c.m.}$= 48.8 to 69.5 MeV. The optical model analysis assumes both phenomenological and folding model potentials. Regions of sensitivity, where the potential is well determined, are found to be different for the real and the imaginary parts, and to vary with energy. The values of the real potential in the surface are weakly dependent on energy.

PACS number(s): 25.70.−z, 25.70.Bc

I. INTRODUCTION

Some recent analyses of heavy-ion elastic scattering measurements have shown rapid variations with energy in the strengths of the nuclear optical potential in the vicinity of the top of the Coulomb barrier. There is a rapid increase in the absorptive strength, accompanied by a rapid decrease in the strength of the real potential, as the energy increases above the Coulomb barrier. This effect has been referred to as a threshold anomaly (see, for example, Ref. [1], for a review) and has been interpreted as due to the increase in importance of couplings to various reaction channels in this energy range. The variations with energy of the real and imaginary parts of the potential are expected to be correlated through a dispersion relation that arises from causality.

The effect has been observed most clearly for ^{16}O+^{208}Pb [1, 2], where a decrease in the real potential strength of nearly a factor of 2 is seen as the energy rises to about 40 MeV above the Coulomb barrier. Weaker dependences on energy have been observed for other systems, such as ^{32}S+^{32}S [3], ^{32}S+^{40}Ca [4], and ^{35,37}Cl+^{24}Mg [5], etc. In order to extend the variety of systems studied, we have measured the elastic scattering of ^{58}Ni+^{27}Al at five energies, up to 20 MeV in the c.m. above the Coulomb barrier. The scattering for the neighboring systems ^{28}Si+^{58,62,64}Ni has been measured by Sugiyama *et al.* [6, 7], who found an important isotopic dependence in their results [7]; an energy dependence was present for ^{64}Ni, but not for ^{58}Ni. This was associated with differences in the importance of neutron transfer reactions in the two cases.

II. MEASUREMENTS

The measurements were carried out with beams of ^{58}Ni from the Holifield Heavy-Ion Research Facility 25-MV tandem at Oak Ridge National Laboratory (ORNL), at laboratory energies of 155, 160, 170, 185, and 220 MeV, which correspond (after energy losses in the 100 μg/cm^2 thick Al target are taken into account) to center-of-mass energies equal to 48.8, 50.4, 53.6, 58.3, and 69.5 MeV, respectively. The Coulomb barrier for this system is about 50 MeV. Because of the reverse kinematics, c.m. angles between 30° and 165° were measured by covering a laboratory angular range between 7° and 51°. The nickel as well as the aluminum ejectiles were momentum analyzed by an Enge split-pole spectrograph equipped with a heavy-ion detection system [8] consisting of two position-sensing proportional counter wires and two ionization chambers. The ejectiles trajectories (angle of incidence at the detector front and position on the spectrograph focal plane) were calculated from the wire information, and the energy loss and total energy were given by the ionization chamber signals. With this system, the kinetic energy, mass, and charge of the reaction products were determined. The entrance slits of the spectrograph were opened 0.69° (FWHM) horizontally subtending a solid angle of 0.51 msr. A Si detector at a fixed forward angle (45° at the lower four energies, and 15.5° at the highest, where the scattering is assumed to be given by the Rutherford cross section) provided relative normalization factors.

Figure 1 shows a typical aluminum spectrum on the calculated focal plane of the spectrograph obtained at one of the backward c.m. angles. The focusing of three charge states is clearly visible and the contribution from inelastic scattering is seen to the left of the elastic peak. The energy resolution of the focal plane spectra was about 1.2 MeV (FWHM) due mostly to energy loss and straggling of the ions through the target and detector. Correction of the observed yields for the atomic charge-state distribution was done according to calculations based on Ref. [9]. The detection efficiency predictions were checked at selected energies during the experiment (changing the magnetic field of the spectrograph so that different charge states would be focused on the focal plane) and the agreement was within 2%.

*Deceased.

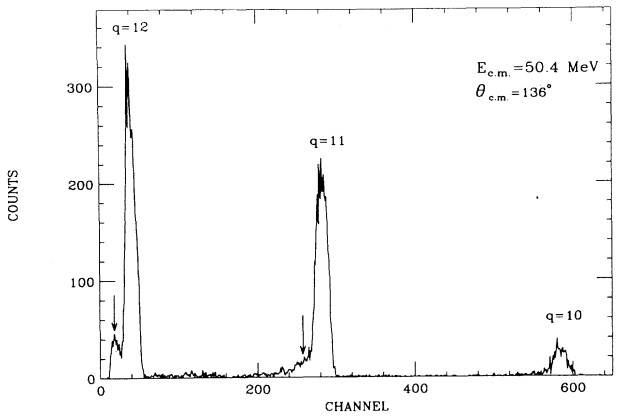

FIG. 1. Aluminum ions projected on the magnet focal plane. Three different charge states q are visible; the contribution from inelastic scattering to the 0.84 MeV state in ^{27}Al is seen to the left of the elastic peaks. The arrows indicate the resolved inelastic peaks.

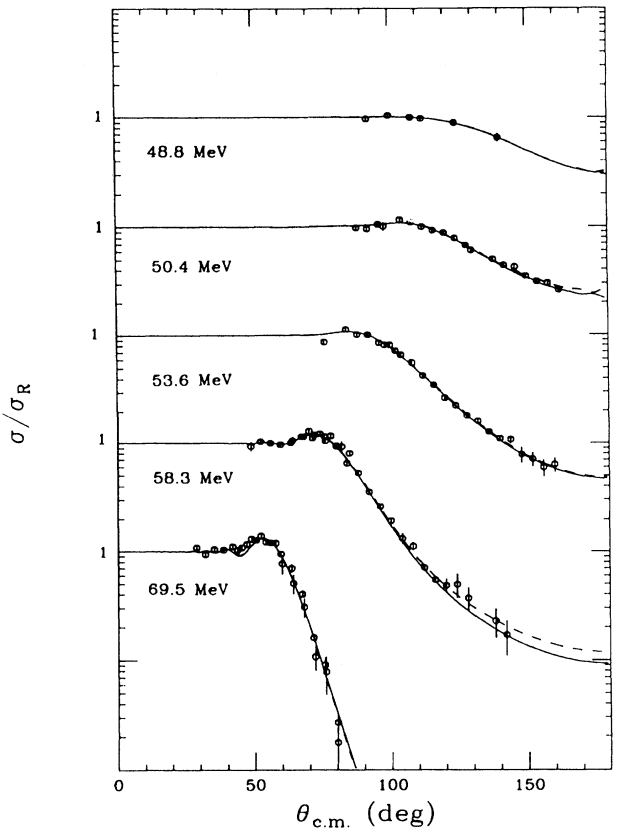

FIG. 2. Elastic scattering differential cross sections (ratio to Rutherford) at the indicated c.m. energies. Solid curves correspond to the phenomenological analysis (parameters P in Table I), and dashed curves, to the folding model analysis (parameters FM in Table I).

Figure 2 shows the angular distributions of the elastic scattering in ratio to the Rutherford cross section. Absolute values of the cross section were derived by normalizing the forward angle yields to Rutherford scattering. The estimated overall uncertainty of the data is 10%. Error bars in Fig. 2 include uncertainties from the elastic peak identification, detection efficiency corrections, and statistics.

III. OPTICAL MODEL ANALYSIS

The optical model analysis of the data was performed assuming both phenomenological and folding model nuclear potentials. Several prescriptions were tried in the phenomenological study. First, the optical model fits assumed Woods-Saxon potentials

$$U(r) = V(r) + iW(r), \tag{1}$$

where $V(r)$ and $W(r)$ have the Woods-Saxon form,

$$V(r) = \frac{-V_0}{1+\exp[(r-R_V)/a_V]} \tag{2}$$

and similarly for $W(r)$. The potential radii R_i, with $i = V$ or W, are taken to be

$$R_i = r_i(A_1^{1/3} + A_2^{1/3}). \tag{3}$$

The study showed that potentials having different form factors for the real and the imaginary parts gave good fits to the data, provided that the imaginary diffuseness a_W was allowed to be small (about 0.3 fm) at all energies. A continuous ambiguity in the determination of the real part allowed us to find a "radius of sensitivity," which corresponds to the radius at which the real part of potentials giving "equally good" fits cross (have the same value). The radii of sensitivity for the real part were found to be about 10.3, 10.6, 10.8, 10.5, and 10.2 fm, respectively, in order of increasing energy. The radii where the imaginary parts of these equally good potentials cross, however, showed a dramatic energy dependence, being equal to 11.4 fm at the lowest energy and about 10.2–10.6 fm at the others (reduced r_W values of 1.66 and 1.48–1.54, respectively). An example of these crossing points is shown in Fig. 3 for $E_{c.m.}$= 48.8 MeV.

Following Ref. [10], we performed an analysis of the data assuming a potential of the form

$$U(r) = V(r) + i[W_F(r) + W_D(r)], \tag{4}$$

where the real potential $V(r)$ has a Woods-Saxon shape, $W_F(r)$ is a short-range (r_W=1.0 fm, a_W=0.25 fm) volume (Woods-Saxon) term that represents fusion after penetration of the barrier, and $W_D(r)$ is a surface (Woods-Saxon derivative) term that represents absorption into direct channels as well as multistep fusion occuring after excitation into quasielastic channels,

$$W_D(r) = 4W_{D0}a_D\frac{d}{dr}\left(\frac{1}{1+\exp[(r-R_D)/a_D]}\right). \tag{4'}$$

As in Ref. [10], we have fixed the volume imaginary term but varied the surface component to fit the data. Since the data were sensitive to only a limited region of the real

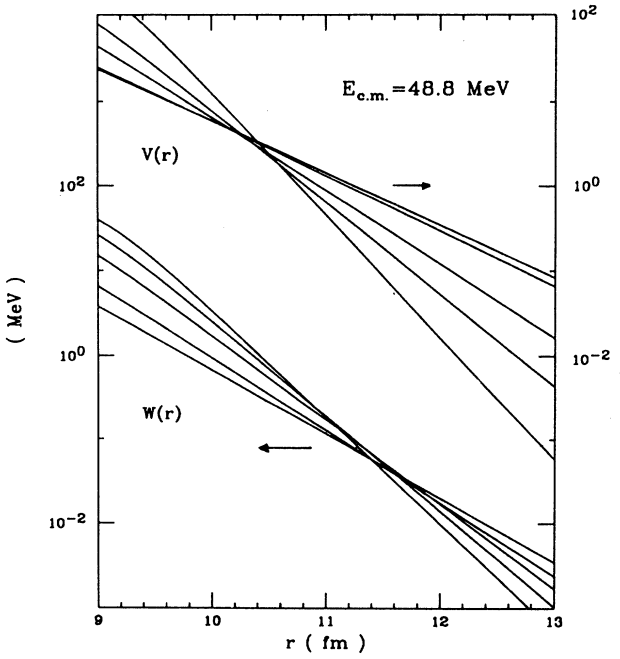

FIG. 3. Real and imaginary parts of Woods-Saxon potentials giving "equally good" fits to the $E_{\rm c.m.}$ =48.8 MeV data.

potential (the surface), the central depth could be fixed at a constant value (the value V_0=250 MeV was chosen) and only the radius and diffuseness varied. Exploratory studies showed that, first, these data are insensitive to the volume component in the imaginary part, and, second, that the location of the surface component displays an energy dependence similar to that of the imaginary crossing radius. Fits to the data at the highest energy required the surface absorption to be centered at a reduced radius r_D smaller than 1.3 fm, while the data for the lowest energy would accept values up to 1.6 fm. We have then assumed an energy dependence for the radius, which is linear for the highest four energies, and about 1 fm larger for the lowest energy. Table I shows the potential parameters (analysis P) and the corresponding calculated cross sections (solid curves) are compared with the experimental ones in Fig. 2.

Next, an analysis using a real potential calculated by double folding the M3Y effective nucleon-nucleon interaction [11] with the nuclear density distributions was performed. The resulting real potential was renormalized by the factor V_0 (Table I), adjusted to optimize the fit to the data. For the imaginary part, the same prescription (4) as above [10] was followed. The entries labeled FM in Table I show the values of the parameters giving optimum fits and dashed curves in Fig. 2 show the corresponding calculations. Only at $E_{\rm c.m.}$=58.3 MeV was there any noticeable difference from the fit obtained with a Woods-Saxon potential.

IV. ENERGY DEPENDENCE OF THE POTENTIAL

Insofar as any apparent energy dependence due to spatial nonlocality can be neglected [12], the energy dependence of the real and the imaginary parts, $V(r,E)$ and $W(r,E)$, respectively, of the complex nuclear potential are expected to be connected by a dispersion relation originating in the causality requirement. In the form used by the authors of Ref. [12], we write $V(r;E) = V_0 + \Delta V(r;E)$, where V_0 is independent of energy; then the dispersion relation can be written

$$\Delta V(r;E) = \frac{P}{\pi}\int \frac{W(r;E')}{E'-E}dE', \qquad (5)$$

where P denotes a principal value.

Previous reports [4, 13] of a rapid variation in the heavy-ion real potential strength near the Coulomb barrier observed in the analysis of elastic scattering data were based on the determination of the real and imaginary potentials at a fixed ("strong absorption") radius $r = R_{\rm SA}$, where the results from the optical model analysis were considered unambiguous. Then Eq.(5) can be directly applied at that radius, $r = R_{\rm SA}$.

In the analysis of the present data, however, the radii where the potentials are well determined by the data are different for the real and imaginary parts (Fig. 3), and also vary with the energy, and the direct application of Eq. (5) is meaningless. On the other hand, the region of

TABLE I. Optical model parameters.

$E_{\rm c.m.}$ (MeV)	Analysis	V_0 (MeV)	r_V (fm)	a_V (fm)	W_{F0} (MeV)	r_F (fm)	a_F (fm)	W_{D0} (MeV)	r_D (fm)	a_D (fm)	χ^2/N
48.8	P	250	1.18	0.418	10	1.0	0.25	1.50	1.55	0.147	0.18
	FM	1.2			10	1.0	0.25	0.384	1.55	0.283	0.19
50.4	P	250	1.11	0.577	10	1.0	0.25	8.54	1.38	0.167	0.87
	FM	1.5			10	1.0	0.25	7.57	1.38	0.151	0.89
53.6	P	250	1.11	0.553	10	1.0	0.25	17.77	1.35	0.277	1.04
	FM	1.1			10	1.0	0.25	13.41	1.35	0.294	1.07
58.3	P	250	1.07	0.628	10	1.0	0.25	35.40	1.305	0.256	0.96
	FM	1.4			10	1.0	0.25	37.57	1.305	0.252	0.99
69.5	P	250	1.10	0.545	10	1.0	0.25	37.67	1.20	0.337	3.8
	FM	1.0			10	1.0	0.25	19.12	1.20	0.388	3.5

sensitivity that we find spans a relatively limited range of radii, so we have used a Gaussian weighting function $G(r)$, centered on some average of the crossing radii, to evaluate the integral quantities $[G(E)]_V$ and $[G(E)]_W$, defined as

$$[G(E)]_V = \frac{1}{58 \times 27} \int V(r;E)G(r)4\pi r^2 dr, \quad (6)$$

and similarly for $[G(E)]_W$. It can easily be seen [12, 14] that the dispersion relation can be extended to any weighting function, and, in particular,

$$\Delta[G(E)]_V = \frac{P}{\pi} \int \frac{[G(E')]_W}{E' - E} dE'. \quad (7)$$

In our case,

$$G(r) = \frac{1}{\sqrt{2\pi}\sigma} \exp\left[-\frac{(r - R_G)^2}{2\sigma^2}\right] \quad (8)$$

with $R_G = 10.5$ fm and $\sigma = 0.5$ fm. This choice should select the important contributions to $[G(E)]_V$ and $[G(E)]_W$ from the region where the potential has been best determined.

Figure 4 shows the values of $[G(E)]_V$ and $[G(E)]_W$ calculated with the phenomenological and folding model potentials. The error bars reflect the rms uncertainty in the parameters as indicated by the optical model fitting program [15], namely changes in the parameters that would result in χ^2 increasing by unity, as well as uncertainties associated to the choice of R_G and σ in Eq. (8). Since the real and imaginary regions of sensitivity are rather narrow at each energy (see Fig. 3), a weighting function wider than the one chosen would include in Eq. (6) contributions from radii where the potential values are not determined by the data. On the other hand, a narrower Gaussian renders difficult the application of the dispersion relation at all energies. The chosen values for R_G and σ represent a compromise, and, after an exploratory study, we have estimated relative uncertainties for each $[G]_V$ and $[G]_W$ arising from their sensitivity to the choice of the Gaussian parameters. The two kinds of uncertainties have been added in quadrature.

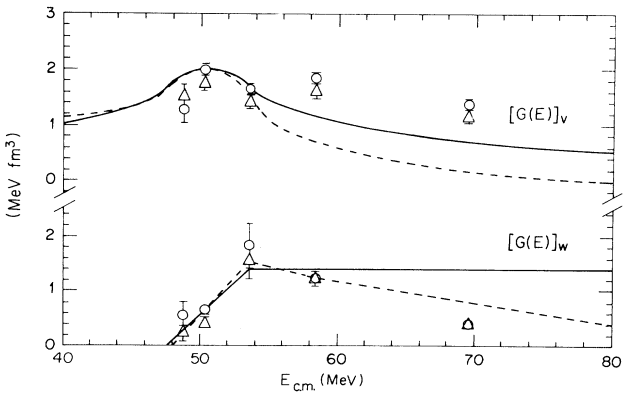

FIG. 4. Values of $[G(E)]_V$ and $[G(E)]_W$, as defined in the text, from the phenomenological (circles) and folding model (triangles) analyses. Solid and dashed curves show two different parametrizations of $[G(E)]_W$, and the corresponding values of $[G(E)]_V$ deduced from the dispersion relation (7) and normalized to the empirical value near 50 MeV.

The curves for $[G(E)]_W$ are two possible parametrizations of the empirical values composed of linear segments, assuming different behaviors at higher energies, while the curves for $[G(E)]_V$ result from using these in the dispersion relation, Eq. (7), normalized to the empirical $[G(E)]_V$ value near 50 MeV.

V. DISCUSSION AND CONCLUSIONS

The observed energy dependence of the real potential shown in Fig. 4 is weaker than what is expected from the dispersion relation, but the uncertainties in the experimental values of $[G(E)]_V$ prevent us from drawing any definitive conclusion. The increase in the absorptive potential $[G(E)]_W$ of 1.5 MeV fm^3 over a range in $E_{\text{c.m.}}$ of about 6 MeV is predicted by Eq. (7) to result in a decrease in $[G(E)]_V$ of about the same amount between the maximum at $E_{\text{c.m.}} \approx 51$ MeV and the highest experimental energy, $E_{\text{c.m.}} \approx 70$ MeV. The observed variation is about half the prediction. This is a decrease of 30%, less than the 40% decrease observed for ^{16}O+^{208}Pb [1, 2] over a similar energy range, but more like the changes inferred, for example, for the projectiles ^{32}S [3, 4] and ^{35,37}Cl [5].

In all the studies of elastic scattering, except ^{16}O+^{208}Pb [1, 2], it has only been possible to infer qualitative support for the existence of a threshold anomaly, and for agreement with the dispersion relations. There are many reasons for this. The most important, perhaps, is the difficulty in determining an optical potential from elastic data as the energy approaches the Coulomb barrier and the angular distributions become featureless. It is well known that strong absorption results in considerable ambiguities in this situation. This is in addition to uncertainties that arise from uncertainties in the experimental data. Furthermore, the magnitude of the anomaly in the real potential depends upon the strengths of the couplings to nonelastic channels, which may vary significantly from system to system.

The strongest evidence for a threshold anomaly in the real potential comes from the enhancement of fusion cross sections at sub- and near-barrier energies [1], which is another manifestation of the increased attraction between the two nuclei at these energies. The simultaneous analysis of fusion cross section and elastic scattering data has been made in a number of cases [1] and has shown overall agreement with expectations based upon the dispersion relation (5). One example is a study of ^{32}S+^{58,64}Ni [16–18], whose results also imply a much larger effect for ^{64}Ni than for ^{58}Ni. However, the empirical anomaly for the real potential is not very well defined in either case, and may be subject to reevaluation in light of new measurements [19] of fusion and elastic scattering in S+Ni below and near the barrier. Certainly, fusion data for ^{58}Ni+^{27}Al could help corroborate our findings from the elastic measurements.

The approach taken in the optical model analysis reported here might be of relevance to the study of the

threshold anomaly in the real potential for other heavy ions. In all cases we know, the dispersion relation (5) has been applied at a specific radius, deduced only from the crossing of the real part of "equally good" potentials. Had we done that [instead of studying the integral quantities (6)] the conclusions would have been quite different, as can be inferred from Fig. 3: the value of $W(r)$ at r =10.4 fm, the crossing radius for $V(r)$, is not determined by the data and depends entirely on the chosen parametrization of the imaginary potential.

In summary, we have measured the elastic angular distributions for ^{58}Ni+^{27}Al at five energies, from the top of the Coulomb barrier to about 20 MeV above it. Optical model analysis of these data indicate that the imaginary potential in the surface rises from a very small value and then levels off for $E_{\mathrm{c.m.}} > 54$ MeV. The associated real potentials are somewhat uncertain, but their variation with energy is weaker than that expected, using the dispersion relation, from the behavior of the imaginary potentials. The "threshold" energy dependence thus inferred is not very marked, but is consistent with those deduced from the scattering of other projectiles of similar mass.

ACKNOWLEDGMENTS

ORNL is operated by Martin Marietta Energy Systems, Inc. under Contract No. DE-AC05-84OR21400 with the U.S. Department of Energy. M.E.B. and A.M-R. were also supported by the Joint Institute for Heavy Ion Research, Holifield Heavy Ion Research Facility, Oak Ridge, Tennessee 37831. J.R.A. acknowledges support from DGAPA-UNAM.

[1] G.R. Satchler, Phys. Rep. **199**, 147 (1991).
[2] M.A. Nagarajan, C. Mahaux, and G.R. Satchler, Phys. Rev. Lett. **54**, 1136 (1985).
[3] B. Bilwes *et al.*, Nucl. Phys. **A473**, 353 (1987).
[4] J. Díaz *et al.*, Nucl. Phys. **A494**, 311 (1989).
[5] J.M. Barrigón *et al.*, Nucl. Phys. **A545**, 720 (1992).
[6] Y. Sugiyama *et al.*, Phys. Lett. B **176**, 302 (1986).
[7] Y. Sugiyama *et al.*, Phys. Rev. Lett. **62**, 1727 (1989).
[8] D. Shapira *et al.*, Nucl. Instrum. Methods **169**, 77 (1980).
[9] K. Shima, T. Ishihara, and T. Mikumo, Nucl. Instrum. Methods **200**, 605 (1982).
[10] G.R. Satchler, M.A. Nagarajan, J.S. Lilley, and I.J. Thompson, Phys. Rev. C **41**, 1869 (1990).
[11] G.R. Satchler and W.G. Love, Phys. Rep. **55**, 183 (1979).
[12] C. Mahaux, H. Ngo, and G.R. Satchler, Nucl. Phys. **A449**, 354 (1986).
[13] D. Abriola *et al.*, Phys. Rev. C **39**, 546 (1989).
[14] C. Mahaux, H. Ngo, and G.R. Satchler, Nucl. Phys. **A456**, 134 (1986).
[15] Code PTOLEMY, M.H. Macfarlane and S.C. Pieper, Argonne National Laboratory Report No. ANL-76-11, 1978 (unpublished).
[16] A.M. Stefanini *et al.*, Phys. Rev. Lett. **59**, 2852 (1987).
[17] A.M. Stefanini *et al.*, Phys. Rev. C **39**, 1840 (1989).
[18] T. Udagawa, T. Tamura, and B.T. Kim, Phys. Rev. C **39**, 1840 (1989).
[19] R.J. Tighe *et al.*, Phys. Rev. C **42**, 1530 (1990).